*Inorg. Chem.* **2000,** *39,* 5697−5706

# Electronic Structure Studies of Oxomolybdenum Tetrathiolate Complexes: Origin of Reduction Potential Differences and Relationship to Cysteine−Molybdenum Bonding in Sulfite Oxidase

**Rebecca L. McNaughton,[†] A. Alex Tipton,[‡] Nick D. Rubie,[†] Rebecca R. Conry,*[,‡] and Martin L. Kirk*[,†]**

Department of Chemistry, The University of New Mexico, Albuquerque, New Mexico 87131-1096, and Department of Chemistry, University of Nevada, Reno, Reno, Nevada 89577-0020

*Received April 6, 2000*

Electronic absorption, magnetic circular dichroism, and resonance Raman spectroscopies have been used to determine the nature of oxomolybdenum−thiolate bonding in $(PPh_4)[MoO(SPh)_4]$ (SPh = phenylthiolate) and $(HNEt_3)[MoO(SPh-PhS)_2]$ (SPh−PhS = biphenyl-2,2′-dithiolate). These compounds, like all oxomolybdenum tetraarylthiolate complexes previously reported, display an intense low-energy charge-transfer feature that we have now shown to be comprised of multiple S → Mo $d_{xy}$ transitions. The integrated intensity of this low-energy band in $[MoO(SPh)_4]^-$ is approximately twice that of $[MoO(SPh\text{-}PhS)_2]^-$, implying a greater covalent reduction of the effective nuclear charge localized on the molybdenum ion of the former and a concomitant negative shift in the Mo(V)/Mo(IV) reduction potential brought about by the differential S → Mo $d_{xy}$ charge donation. However, this is not observed experimentally; the Mo(V)/Mo(IV) reduction potential of $[MoO(SPh)_4]^-$ is ∼120 mV *more positive* than that of $[MoO(SPh-PhS)_2]^-$ (−783 vs −900 mV). Additional electronic factors as well as structural reorganizational factors appear to play a role in these reduction potential differences. Density functional theory calculations indicate that the electronic contribution results from a greater $\sigma$-mediated charge donation to unfilled higher energy molybdenum acceptor orbitals, and this is reflected in the increased *energies* of the $[MoO(SPh-PhS)_2]^-$ ligand-to-metal charge-transfer transitions relative to those of $[MoO(SPh)_4]^-$. The degree of S−Mo $d_{xy}$ covalency is a function of the O≡Mo−S−C dihedral angle, with increasing charge donation to Mo $d_{xy}$ and increasing charge-transfer intensity occurring as the dihedral angle decreases from 90 to 0°. These results have implications regarding the role of the coordinated cysteine residue in sulfite oxidase. Although the O≡Mo−S−C dihedral angles are either ∼59 or ∼121° in these oxomolybdenum tetraarylthiolate complexes, the crystal structure of the enzyme reveals an $O{\equiv}Mo{-}S_{Cys}{-}C$ angle of ∼90°. Thus, a significant reduction in $S_{Cys}$−Mo $d_{xy}$ covalency is anticipated in sulfite oxidase. This is postulated to preclude the direct involvement of coordinated cysteine in coupling the active site into efficient superexchange pathways for electron transfer, provided the $O{\equiv}Mo{-}S_{Cys}{-}C$ angle is not dynamic during the course of catalysis. Therefore, we propose that a primary role for coordinated cysteine in sulfite oxidase is to statically poise the reduced molybdenum center at more negative reduction potentials in order to thermodynamically facilitate electron transfer from Mo(IV) to the endogenous b-type heme.

## Introduction

The majority of pyranopterin molybdenum enzymes catalyze specific two-electron redox reactions that are coupled to formal oxygen atom transfer. Considerable insight into the mechanism of both the oxidative and reductive half-reactions has been derived from spectroscopic and mechanistic studies on the enzymes and relevant biomimetic model compounds.[1,2] Spectroscopic studies of oxomolybdenum ene-1,2-dithiolate complexes[3−5] and the xanthine oxidase[6] “very rapid” intermediate suggest that electron-transfer (ET) regeneration of the molybdenum active site occurs via an “oxo-gate” mechanism. This oxo-gate hypothesis states that an ene-1,2-dithiolate chelate oriented cis to a single Mo≡O group is a necessary prerequisite for ET regeneration in pyranopterin enzymes. Evidence continues to mount in support of the ene-1,2-dithiolate coupling the active site into efficient $\sigma$-type superexchange pathways involving the pyranopterin.[4−6] Interestingly, this ET hypothesis is put to the test in sulfite oxidase (SO). SO possesses two different sulfur donor types, namely, the aforementioned ene-1,2-dithiolate and a single cysteine thiolate ($S_{Cys}$), both of which are capable of being directly involved in the ET regeneration process. A recent crystal structure of chicken liver SO[7] coupled with numerous spectroscopic studies including XAS,[8−11] reso-

---

* To whom correspondence should be addressed.

[†] The University of New Mexico.

[‡] University of Nevada, Reno.

(1) Hille, R. *Chem. Rev.* **1996**, *96*, 2757−2816.

(2) Enemark, J. H.; Young, C. G. *Adv. Inorg. Chem.* **1993**, *40*, 1−88.

(3) Carducci, M. D.; Brown, C.; Solomon, E. I.; Enemark, J. H. *J. Am. Chem. Soc.* **1994**, *116*, 11856−11868.

(4) Inscore, F. E.; McNaughton, R.; Westcott, B. L.; Helton, M. E.; Jones, R.; Dhawan, I. K.; Enemark, J. H.; Kirk, M. L. *Inorg. Chem.* **1999**, *38*, 1401−1410.

(5) McNaughton, R. L.; Helton, M. E.; Rubie, N. D.; Kirk, M. L. *Inorg. Chem.* **2000**, *39*, 4386−4387.

(6) Jones, R. M.; Inscore, F. E.; Hille, R.; Kirk, M. L. *Inorg. Chem.* **1999**, *38*, 4963−4970.

(7) Kisker, C.; Schindelin, H.; Pacheco, A.; Wehbi, W. A.; Garrett, R. M.; Rajagopalan, K. V.; Enemark, J. H.; Rees, D. C. *Cell* **1997**, *91*, 973−983.

(8) George, G. N.; Garrett, R. M.; Prince, R. C.; Rajagopalan, K. V. *J. Am. Chem. Soc.* **1996**, *118*, 8588−8592.

10.1021/ic0003729 CCC: $19.00

**Scheme 1.** Proposed Catalytic Mechanism of SO Showing the Geometries of the Oxidized, Reduced, and ET-Relevant Forms of the Mo Active Sites (the Abbreviated Dithiolate Ligand Represents the Pyranopterin Ene-1,2-dithiolate)

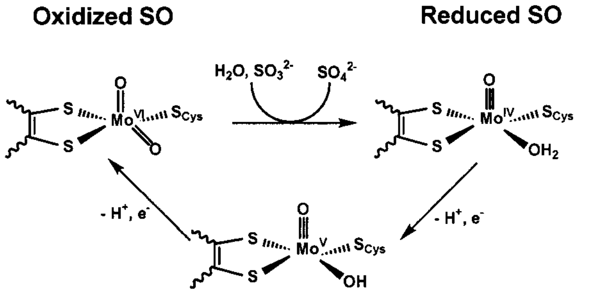

nance Raman,[12] EPR,[13−17] ESEEM,[18,19] and electronic absorption[20,21] have led to a detailed description of the molybdenum active site coordination geometry and a proposed catalytic mechanism (Scheme 1).[1,22] The reduced Mo(IV) and Mo(V) sites are believed to adopt a square-pyramidal geometry with a single oxo ligand located in the apical position. The three equatorial sulfur donors remain coordinated to molybdenum during the course of catalysis, in contrast to the equatorial oxo ligand which is replaced by a coordinated water or hydroxide ligand upon reduction. Mechanistically, the two-electron oxidation of sulfite in SO is believed to involve formal oxygen atom transfer via an initial attack of the sulfite sulfur lone pair on the equatorial Mo≡O bond to generate a 2e$^-$-reduced Mo(IV) intermediate. Under turnover conditions, this intermediate is reoxidized to the resting Mo(VI) state by two sequential one-electron transfers to cytochrome *c*, the physiological oxidant, via an endogenous b-type heme.

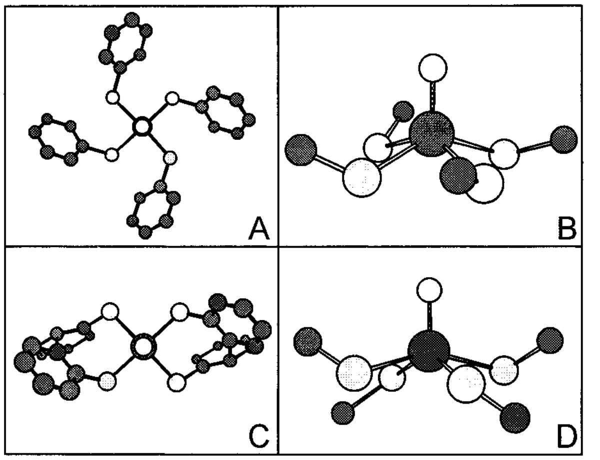

**Figure 1.** Pictures of the solid-state structures of **1** and **2**. (A) Top view of **1**. (B) Side view of the $MoOS_4C_4$ core of **1**. (C) Top view of **2**. (D) Side view of the $MoOS_4C_4$ core of **2**. H atoms have been omitted for clarity.

**Table 1.** Selected Bond Lengths, Bond Angles, and Dihedral Angles

| | $[MoO(SPh)_4]^-$ ($1^a$) | $[MoO(SPh\text{-}PhS)_2]^-$ ($2^b$) |
|---|---|---|
| | Bond Lengths (Å) | |
| Mo−O | 1.669 | 1.684 |
| Mo−S1 | 2.401 | 2.388 |
| Mo−S2 | 2.401 | 2.406 |
| Mo−S3 | 2.397 | 2.395 |
| Mo−S4 | 2.411 | 2.387 |
| | Bond Angles (deg) | |
| Mo−S1−C | 107.3 | 116.0 |
| Mo−S2−C | 111.4 | 100.9 |
| Mo−S3−C | 111.7 | 116.7 |
| Mo−S4−C | 108.8 | 99.4 |
| O−Mo−S1 | 110.2 | 109.5 |
| O−Mo−S2 | 108.5 | 103.9 |
| O−Mo−S3 | 111.2 | 110.9 |
| O−Mo−S4 | 109.5 | 104.0 |
| S1−Mo−S2 | 85.6 | 91.6 |
| S2−Mo−S3 | 83.4 | 78.4 |
| S3−Mo−S4 | 82.1 | 90.6 |
| S4−Mo−S1 | 82.5 | 80.2 |
| | Dihedral Angles (deg) | |
| O−Mo−S1−C | 57.4 | −121.8 |
| O−Mo−S2−C | 62.8 | 51.9 |
| O−Mo−S3−C | 61.0 | −120.4 |
| O−Mo−S4−C | 53.9 | 51.1 |

[a] Reference 26. [b] Reference 39.

As a result of the important role coordinated cysteine plays in ET processes facilitated by blue copper proteins,[23,24] we have begun investigating oxomolybdenum complexes which possess alkyl- and arylthiolate ligands as models for Mo−$S_{Cys}$ bonding in SO. The $[MoO(SR)_4]^{n-}$ oxomolybdenum thiolates were among the earliest inorganic complexes put forth as potential models for pyranopterin molybdenum enzyme active sites, and these complexes have been shown to display intense ligand-to-metal charge-transfer (LMCT) transitions, which have been broadly attributed to S → Mo charge-transfer processes.[25−37] We have conducted a detailed electronic structure study of $(PPh_4)[MoO(phenylthiolate)_4]$ (**1**) and $(HNEt_3)[MoO(biphenyl\text{-}2,2'\text{-}dithiolate)_2]$ (**2**; see Figure 1 and Table 1), and have found that second coordination-sphere effects are especially important in determining the degree of orbital overlap in the Mo−$S_{thiolate}$

---

(9) George, G. N.; Pickering, I. J.; Kisker, C. *Inorg. Chem.* **1999**, *38*, 2539−2540.
(10) George, G. N. Kipke, C. A.; Prince, R. C.; Sunde, R. A.; Enemark, J. H.; Cramer, S. P. *Biochemistry* **1989**, *28*, 5075−5080.
(11) Cramer, S. P.; Wahl, R.; Rajagopalan, K. V. *J. Am. Chem. Soc.* **1981**, *103*, 7721−7727.
(12) Garton, S. D.; Garrett, R. M.; Rajagopalan, K. V.; Johnson, M. K. *J. Am. Chem. Soc.* **1997**, *119*, 2590−2591.
(13) Dhawan, I. K.; Enemark, J. H. *Inorg. Chem.* **1996**, *35*, 4873−4882.
(14) Lamy, M. T.; Gutteridge, S.; Bray, R. C. *Biochem. J.* **1980**, *185*, 397−403.
(15) Gutteridge, S.; Lamy, M. T.; Bray, R. C. *Biochem. J.* **1980**, *191*, 285−288.
(16) Bray, R. C.; Gutteridge, S.; Lamy, M. T.; Wilkinson, T. *Biochem. J.* **1983**, *211*, 227−236.
(17) George, G. N.; Prince, R. C.; Kipke, C. A.; Sunde, R. A.; Enemark, J. H. *Biochem. J.* **1988**, *256*, 307−309.
(18) Pacheco, A.; Basu, P.; Borbat, P.; Raitsimring, A. M.; Enemark, J. H. *Inorg. Chem.* **1996**, *35*, 7001−7008.
(19) Raitsimring, A. M.; Pacheco, A.; Enemark, J. H. *J. Am. Chem. Soc.* **1998**, *120*, 11263−11278.
(20) Johnson, J. L.; Rajagopalan, K. V. *J. Biol. Chem.* **1977**, *252*, 2017−2025.
(21) Garrett, R. M.; Rajagopalan, K. V. *J. Biol. Chem.* **1996**, *271*, 7387−7391.
(22) Brody, M. S.; Hille, R. *Biochemistry* **1999**, *38*, 6668−6677.
(23) Solomon, E. I.; Baldwin, M. J.; Lowery, M. D. *Chem. Rev.* **1992**, *92*, 521−542 and references therein.
(24) Holm, R. H.; Kennepohl, P.; Solomon, E. I. *Chem. Rev.* **1996**, *96*, 2239−2314 and references therein.
(25) Ueyama, N.; Yoshinaga, N.; Okamura, T.; Zaima, H.; Nakamura, A. *J. Mol. Catal.* **1991**, *64*, 247−256.
(26) Bradbury, J. R.; Mackay, M. F.; Wedd, A. G. *Aust. J. Chem.* **1978**, *31*, 2423−2430.
(27) Bradbury, J. R.; Wedd, A. G.; Bond, A. M. *J. Chem. Soc., Chem. Commun.* **1979**, 1022−1025.
(28) Bradbury, J. R.; Masters, A. F.; McDonell, A. C.; Brunette, A. A.; Bond, A. M.; Wedd, A. G. *J. Am. Chem. Soc.* **1981**, *103*, 1959−1964.
(29) Huang, J.; Ostander, R. L.; Rheingold, A. L.; Walters, M. A. *Inorg. Chem.* **1995**, *34*, 1090−1093.
(30) Soong, S.-L.; Chebolu, V.; Koch, S. A.; O'Sullivan, T.; Millar, M. *Inorg. Chem.* **1986**, *25*, 4067−4068.

bonding scheme. These second coordination-sphere effects manifest themselves in rather unique ways to impart specific functions in metalloproteins. For example, the blue copper proteins possess a highly covalent $S_{Cys}-Cu$ $d_{x^2-y^2}$ $\pi$-bonding interaction that is a direct result of the $S_{Met}-Cu-S_{Cys}-C$ dihedral angle being ~0° (the $Cu-S_{Cys}-C$ plane is orthogonal to the $N_{His}-Cu-N_{His}$ plane).[38] It is the orientation of the carbon directly bound to the cysteine sulfur donor that orients a $S_{Cys}$ p orbital for maximum $\pi$ overlap with the Cu $d_{x^2-y^2}$ orbital. The present study reveals that the nature of $Mo-S_{thiolate}$ bonding is highly dependent on the $O\equiv Mo-S-C$ dihedral angle, and it is this angle which determines the degree to which the thiolate S 3p orbitals interact with the oxo-Mo $d_{xy}$ redox-active orbital. Additionally, we find that substantial $\sigma$-mediated charge donation to higher energy acceptor orbitals localized on molybdenum results in thermodynamic stabilization of the Mo(V) oxidation state to reduction. Hence, we postulate that a primary role of $S_{Cys}$ in SO is to statically poise the reduced molybdenum active site at more negative reduction potentials in order to thermodynamically facilitate ET regeneration of the oxidized Mo(VI) active site.

## Experimental Section

**General Procedures.** All reactions were carried out in an inert atmosphere of $N_2$ using standard Schlenk techniques, and all solvents were dried and deoxygenated prior to use. The compounds **1**[27] and **2**[39] were prepared as previously described. All spectroscopic samples were prepared in a glovebag under a $N_2$ stream in order to ensure sample integrity.

**Electronic Absorption Spectroscopy.** Solution electronic absorption spectra were collected on a Hitachi U-3501 UV−vis−NIR spectrophotometer using a single-beam configuration at 2.0 nm resolution. Samples were prepared by dissolving the compounds in $CH_3CN$, and all spectra were collected at room temperature in a 1 cm anaerobic cell.

**Magnetic Circular Dichroism (MCD) Spectroscopy.** Low-temperature MCD spectra were collected on a system consisting of a Jasco J600 CD spectropolarimeter, employing Hamamatsu photomultiplier tubes of either S-1 or S-20 response, an Oxford Instruments SM4000-7T superconducting magnetooptical cryostat (0−7 T, 1.4−300 K), and an ITC503 Oxford Instruments temperature controller. The spectrometer was calibrated for circular dichroism intensity with camphorsulfonic acid, and the wavelength was calibrated using Nd-doped glass. Samples were prepared by dissolving the compounds in 10:1 2-methyl-THF/DMF and injecting the solution into a ring septum fitted between two 1 mm Infrasil quartz disks housed in a custom-designed sample cell. Monitoring of the depolarization of the incident radiation was accomplished by comparing the intrinsic circular dichroism of a standard Ni (+)-tartrate solution positioned in front of, and then in back of, each sample. The spectra were collected at 2.0 nm resolution at a temperature of 5 K in an applied magnetic field of 7 T.

**Resonance Raman Spectroscopy.** Coherent Innova 70-5 (5 W) $Ar^+$ ion and Innova 300C $Kr^+$ ion lasers were used as the excitation sources, and the scattered radiation was dispersed onto a liquid-$N_2$-cooled 1 in. Spex Spectrum One CCD detector using a Spex 1877E triple-grating monochromator equipped with 600, 1200, and 1800 gr/mm holographic gratings at the spectrographic stage. The laser power at the sample was kept below ~60 mW to prevent thermal degradation of the sample. Samples were prepared by dissolving the compounds in $CH_2Cl_2$ and sealing the solutions in NMR tubes. Raman spectra were obtained with the sample tube placed in a modified NMR sample holder/spinner. Relative resonance enhancement ratios were determined by comparing the integrated intensity of a Raman band at a given excitation wavelength relative to that of the 702 $cm^{-1}$ band of $CH_2Cl_2$.

**Electrochemistry.** Cyclic voltammetry measurements were performed using a BAS-50W potentiostat, employing a platinum disk and platinum wire as the working and auxiliary electrodes, respectively. The potentials were measured relative to a saturated calomel reference electrode and reported versus a ferrocene/ferrocenium internal standard. The potential of the ferrocene/ferrocenium couple was at +428 mV in this cell under the same conditions. The supporting electrolyte was $[n\text{-}Bu_4N][PF_6]$ at a concentration of 0.1 M. Sample concentrations were $\sim 3.0 \times 10^{-3}$ M in $CH_3CN$, and a scan rate of 100 mV/s was typically used.

**Density Functional Theory (DFT) Calculations .** DFT calculations were performed using the Gaussian 98W[40] software package running on a 550 MHz Dell Pentium III workstation. The B3LYP hybrid functional was used, with a 6-31G basis set on all atoms except molybdenum, where the LANL2DZ basis set was used. The computational model $[MoO(SCH_3)_4]^-$ was employed, with methyl groups replacing the phenyl rings of the phenylthiolate and biphenyl-2,2′-dithiolate ligands in order to minimize run times. Bond lengths and angles for the $MoOS_4C_4$ cores of **1** and **2** were taken from crystallographic data.

## Results

**Electronic Absorption Spectra.** The electronic absorption spectra of **1** and **2** are shown in Figure 2 and are similar to those observed for other oxo-Mo(V)/(VI) tetrathiolate complexes.[31−37] The observed intense low-energy absorption band is characteristic of these complexes and has previously been attributed to a S → Mo LMCT transition ($E_{max} \approx 15\,000-18\,000$ $cm^{-1}$, $\epsilon \approx 3000-6000$ $M^{-1}$ $cm^{-1}$). The spectral features of **2** are shifted approximately 1000 $cm^{-1}$ to higher energy relative to those of **1**, and the reduced intensity and blue shift of the bands in **2** have been observed for other ortho-substituted thiolate complexes.[34−36]

The broad, low-energy absorption band of **1** spans the 13 000−19 000 $cm^{-1}$ region, with a single maximum observed at 16 580 $cm^{-1}$ ($\epsilon \approx 6000$ $M^{-1}$ $cm^{-1}$). No discernible features with appreciable absorption intensity are observed between 19 000 and 24 000 $cm^{-1}$. A very broad absorption envelope is seen above 24 500 $cm^{-1}$, with a well-defined shoulder clearly present at ~30 000 $cm^{-1}$ ($\epsilon \approx 13\,000$ $M^{-1}$ $cm^{-1}$). The spectrum of **2** displays two features below 25 000 $cm^{-1}$, with maxima at 17 530 $cm^{-1}$ ($\epsilon \approx 3400$ $M^{-1}$ $cm^{-1}$) and ~21 000 $cm^{-1}$ ($\epsilon \approx 1500$ $M^{-1}$ $cm^{-1}$). Similar to **1**, a region of low intensity is present (22 000−25 000 $cm^{-1}$) followed by intense absorptions

---

(31) Boyd, I. W.; Dance, I. G.; Murray, K. S.; Wedd, A. G. *Aust. J. Chem.* **1978**, *31*, 279−284.

(32) Hanson, G. R.; Brunette, A. A.; McDonell, A. C.; Murray, K. S.; Wedd, A. G. *J. Am. Chem. Soc.* **1981**, *103*, 1953−1959.

(33) Ueyama, N.; Yoshinaga, N.; Kajiwara, A.; Nakamura, A. *Chem. Lett.* **1990**, 1781−1784.

(34) Ellis, S. R.; Collison, D.; Garner, C. D. *J. Chem. Soc., Dalton Trans.* **1989**, 413−417.

(35) Ueyama, N.; Zaima, H.; Nakamura, A. *Chem. Lett.* **1986**, 1099−1102.

(36) Ueyama, N.; Okamura, T.; Nakamura, A. *J. Am. Chem. Soc.* **1992**, *114*, 8129−8137.

(37) McMaster, J.; Carducci, M. D.; Yang, Y.; Solomon, E. I.; Enemark, J. H. *Inorg. Chem.* In press.

(38) Guckert, J. A.; Lowery, M. D.; Solomon, E. I. *J. Am. Chem. Soc.* **1995**, *117*, 2817−2844.

(39) Tipton, A. A.; Conry, R. R. Manuscript in preparation.

(40) Frisch, M. J.; Trucks, G. W.; Schlegel, H. B.; Scuseria, G. E.; Robb, M. A.; Cheeseman, J. R.; Zakrzewski, V. G.; Montgomery, J. A., Jr.; Stratmann, R. E.; Burant, J. C.; Dapprich, S.; Millam, J. M.; Daniels, A. D.; Kudin, K. N.; Strain, M. C.; Farkas, O.; Tomasi, J.; Barone, V.; Cossi, M.; Cammi, R.; Mennucci, B.; Pomelli, C.; Adamo, C.; Clifford, S.; Ochterski, J.; Petersson, G. A.; Ayala, P. Y.; Cui, Q.; Morokuma, K.; Malick, D. K.; Rabuck, A. D.; Raghavachari, K.; Foresman, J. B.; Cioslowski, J.; Ortiz, J. V.; Baboul, A. G.; Stefanov, B. B.; Liu, G.; Liashenko, A.; Piskorz, P.; Komaromi, I.; Gomperts, R.; Martin, R. L.; Fox, D. J.; Keith, T.; Al-Laham, M. A.; Peng, C. Y.; Nanayakkara, A.; Gonzalez, C.; Challacombe, M.; Gill, P. M. W.; Johnson, B.; Chen, W.; Wong, M. W.; Andres, J. L.; Gonzalez, C.; Head-Gordon, M.; Replogle, E. S.; Pople, J. A. *Gaussian 98*, Revision A.7; Gaussian, Inc.: Pittsburgh, PA, 1998.

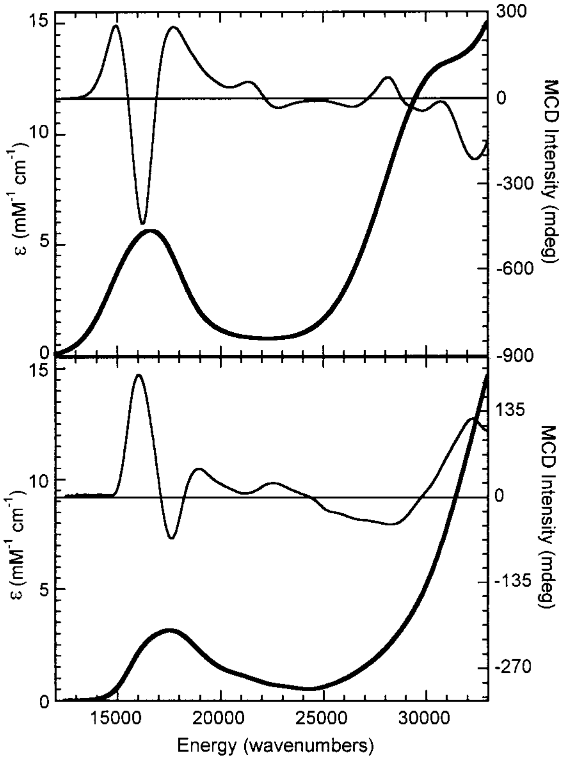

**Figure 2.** Solution electronic absorption (thick line) and MCD (thin line) spectra of **1** (top) and **2** (bottom).

above 25 000 cm$^{-1}$. However, no high-energy shoulder is observed on this absorption edge, indicating this band has probably shifted to higher energy relative to that observed in **1**.

**MCD Spectra.** The 5 K MCD spectra of **1** and **2** are overlayed on their respective absorption spectra in Figure 2. The MCD spectrum of **2** is shifted approximately 1000 cm$^{-1}$ to higher energy relative to **1**, paralleling the absorption data. The observed MCD dispersion consists of both C-term and pseudo A-term components.[41] Both complexes display three MCD bands with a positive−negative−positive pattern located under the envelope of the broad, low-energy absorption feature. This MCD band pattern could arise from three individual C-terms or a single C-term and a pseudo A-term. The latter situation is anticipated because the pseudo $C_4$ symmetry results in specific ligand-based molecular orbitals being degenerate. The similarity of the MCD spectra for these two complexes diverges above 21 000 cm$^{-1}$, where **1** displays a very symmetric negative pseudo A-term feature at 22 000 cm$^{-1}$, and **2** possesses a weak positive band at 22 000 cm$^{-1}$ followed by a weak negative band at 25 500 cm$^{-1}$. These differences are consistent with the observed lower symmetry of **2**.

**Resonance Raman Spectroscopy.** Solution resonance Raman spectra of **1** and **2** were collected using laser excitation wavelengths of 406.7 nm (24 588 cm$^{-1}$), 476.6 nm (20 986 cm$^{-1}$), 568.2 nm (17 599 cm$^{-1}$), and 647.1 nm (15 439 cm$^{-1}$). These wavelengths span the entire energy region of the low-energy absorption features of both complexes. A summary of the observed vibrational modes is listed in Table 2. Four vibrations are observed below 500 cm$^{-1}$ and are tentatively assigned as Mo−thiolate modes. The Mo≡O stretch is observed at 939 cm$^{-1}$ for **1** and 948 cm$^{-1}$ for **2**, within the typical experimental range for mono-oxomolybdenum thiolate complexes.[4,33−35]

**Table 2.** Summary of Raman Frequencies (cm$^{-1}$) for **1** and **2**

| band | **1** | **2** | assignment |
|---|---|---|---|
| $\nu_1$ | 366 | 375 | Mo−S stretch |
| $\nu_2$ | 405 | | |
| $\nu_3$ | 425 | 423 | Mo−S stretch |
| $\nu_4$ | | 454 | |
| $\nu_5$ | 480 | 482 | |
| $\nu_6$ | 566 | 566 | |
| $\nu_7$ | 939 | 948 | Mo≡O stretch |

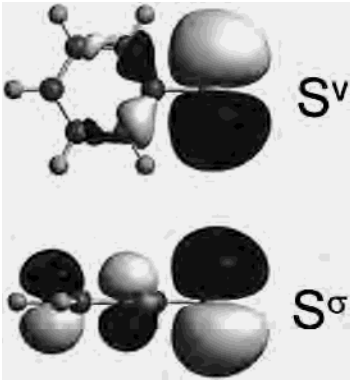

**Figure 3.** Molecular-orbital contour plots of the two highest energy occupied orbitals of the PhS$^-$ ligand. The S 3p orbital of the S$^\sigma$ molecular orbital is orthogonal to the phenyl-ring plane and forms $\sigma$ bonds with Mo. The S 3p orbital of the S$^v$ molecular orbital is parallel to the phenyl-ring plane.

**Electrochemistry.** The Mo(V)/Mo(IV) reduction potentials of **1** and **2** are −783 and −900 mV versus ferrocene/ferrocenium, respectively. Previous studies show that changes in the reduction potential, relative to **1**, are greatest for phenylthiolate donors possessing electron-withdrawing substituents[27,28,30,34,35] or ortho-substituted amide groups that form H bonds with the thiolate S donor.[29,36] It is interesting to note that the reduction potential of $(PPh_4)[MoO(benzene\text{-}1,2\text{-}dithiolate)_2]$, which also possesses four thiolate donor ligands, is −368 mV. This points to *substantial* differences in the electron-donating ability of monothiolate ligands when compared to ene-1,2-dithiolate ligands.

**Electronic Structure Calculations.** DFT calculations performed on the phenylthiolate (PhS$^-$) ligand show that the two highest energy occupied molecular orbitals are primarily S 3p in character (Figure 3). These filled orbitals are nearly degenerate, and the calculations reveal that they are energetically isolated by ~2.5 eV from lower energy occupied molecular orbitals. These two S p orbitals are oriented such that they are orthogonal to the S−C$_{\mathrm{ring}}$ bond and orthogonal to each other. An analogous set of S-based molecular orbitals result from calculations of the biphenyl-2,2′-dithiolate (SPh−PhS$^{2-}$) ligand. However, the Mulliken charge per sulfur donor is only comparable between these two ligands when the S−C−C′−S′ torsion angle of SPh−PhS$^{2-}$ is greater than ~55° (Figure S1 in the Supporting Information).[42] Because the S−C−C′−S′ angles are observed to be 63.7 and 65.0° in the crystal structure of **2**, we anticipate a relatively similar intrinsic electron-donating ability for these two ligands despite the ortho substitution of the SPh−PhS$^{2-}$ phenyl rings. The calculated Mulliken charge per sulfur on X$_n$−PhS$^-$ ligands indicates that the electron-

---

(41) C-term features possess intensity maxima that directly correspond to absorption maxima, whereas pseudo-A-term features are derivative-shaped, with zero intensity at the energies corresponding to absorption maxima. See: Piepho, S. B.; Schatz, P. N. *Group Theory in Spectroscopy with Applications to Magnetic Circular Dichroism*; Wiley-Interscience: New York, 1983.

(42) The Mulliken charge on sulfur for PhS$^-$ is −0.629 compared to −0.594 for SPh−PhS$^{2-}$ when the S−C−C′−S′ angle is 65°.

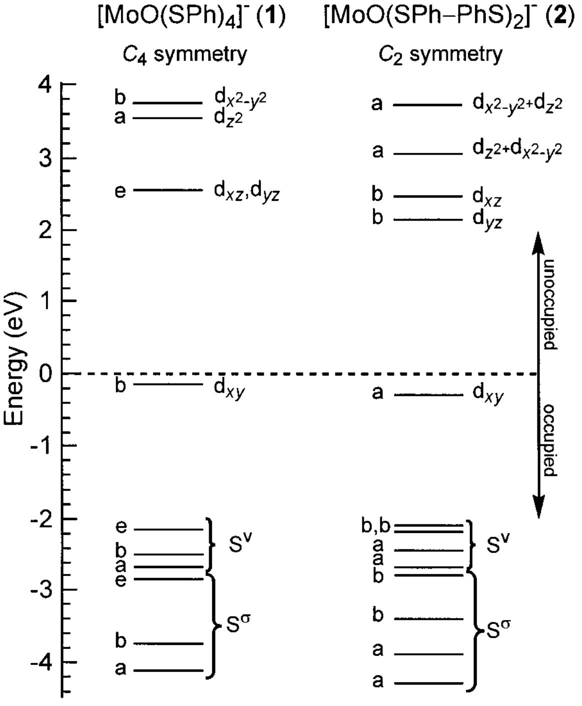

**Figure 4.** Molecular-orbital energy diagram resulting from DFT calculations on $[MoO(SCH_3)_4]^-$ using the crystallographic parameters of **1** and **2** for the $MoOS_4C_4$ cores.

donating/withdrawing properties of the substituent (X) and the number (*n*) of these substituents are more important in affecting the charge on the sulfur than the substitution position on the phenyl ring. This is consistent with electrochemical studies (vide supra), which also indicate that the number of substituents as well as their electronic properties have a greater effect on reduction potentials than simply the substitution position on the ring.

Electronic structure calculations on the $MoOS_4C_4$ core of **1** and **2** were performed using methylthiolate ($CH_3S^-$) ligands in place of each $PhS^-$ donor. The molecular-orbital energy-level diagram shown in Figure 4 depicts the results of calculations performed using the crystallographically determined bond lengths and angles for the two $MoOS_4C_4$ cores. As anticipated, the calculations show that the molybdenum ligand field is dominated by the terminal oxo ligand, resulting in the $d_{xy}$ orbital being lowest in energy and singly occupied. Electron-density contours of $[MoO(SCH_3)_4]^-$ using the crystallographically determined geometry of **1** are presented in Figure 5, and the orbital character of the molybdenum valence orbitals is listed in Table 3. The $C_{4v} \rightarrow C_4$ symmetry reduction in **1** results in an effective rotation of the Mo $d_{xy}$ and $d_{x^2-y^2}$ orbitals off of the Mo−S bond vectors and ensures maximal $S^{\sigma}$−Mo $d_{x^2-y^2}$ orbital overlap in the lower symmetry environment. The DFT calculations for $[MoO(SCH_3)_4]^-$, in the solid-state geometry of **1**, show that 55.5% S character is present in the $d_{x^2-y^2}$ molecular orbital. The $d_{z^2}$, $d_{xz}$, and $d_{yz}$ molecular orbitals possess considerable Mo≡O antibonding character in addition to Mo−S antibonding interactions. In-plane Mo−S bonding is dominated by $S^{\sigma}$−Mo $d_{x^2-y^2}$ $\sigma$ interactions ($S^{\sigma}$(b)) and $S^{v}$−Mo $d_{xy}$ pseudo-$\sigma$ interactions ($S^{v}$(b)). The primarily thiolate-based molecular orbitals are divided into one set composed of four $S^{\sigma}$ orbitals and another containing four $S^{v}$ orbitals. The calculations place all four $S^{\sigma}$ molecular orbitals at deeper binding energies than the $S^{v}$ donor set. The highest energy thiolate-based molecular orbital ($S^{v}$(e)) is weakly antibonding with respect to the oxo $p_x$ and $p_y$ orbitals but does not possess significant molybdenum character. $S^{v}$(a) is stabilized relative to the other $S^{v}$ molecular orbitals by bonding interactions with the oxo $p_z$ orbital. The highest energy $S^{\sigma}$ molecular orbital ($S^{\sigma}$(e)) has the most Mo≡O antibonding character of all of the thiolate-based molecular orbitals, in addition to a bonding interaction with Mo $d_{xz}$ and $d_{yz}$. No substantial oxo or molybdenum character is present in $S^{\sigma}$(a), but a large S−S bonding interaction is present, and this is the dominant contributor to the stabilization of this orbital. The related contours for $[MoO(SCH_3)_4]^-$ in the geometry of **2** are similar in appearance to those depicted in Figure 5 except for the noticeable distortion toward $C_2$ symmetry (Figures 6 and S2 in the Supporting Information). This is especially evident in the $d_{z^2}$, $d_{x^2-y^2}$, and $S^{\sigma}$ molecular orbitals, where the Mo $d_{z^2}$, $d_{xy}$, and $d_{x^2-y^2}$ are allowed to mix by symmetry (these orbitals all possess "a" symmetry in $C_2$). Specifically, this symmetry reduction results in a substantial increase in the sulfur character mixed into the $d_{z^2}$ molecular orbital of **2** (Table 3) and a significant splitting of the $S^{\sigma}$(e) orbitals that were degenerate in $C_4$ symmetry (Figure 4).

**Table 3.** Orbital Character for **1** and **2** Resulting from DFT Calculations

| | molecular orbital character (%) | | | | | | | | |
|---|---|---|---|---|---|---|---|---|---|
| | $[MoO(SPh)_4]^-$ (**1**) | | | | $[MoO(SPh\text{-}PhS)_2]^-$ (**2**) | | | | |
| orbital | Mo | S | O | C | Mo | $S^a$ | $S^b$ | O | C |
| $d_{xy}$ | 68.3 | 26.3 | 0.0 | 3.6 | 69.7 | 7.8 | 14.9 | 0.0 | 5.2 |
| $d_{xz}$ | 54.2 | 21.4 | 17.7 | 4.1 | 55.8 | 0.0 | 18.7 | 18.7 | 3.4 |
| $d_{yz}$ | 54.2 | 21.4 | 17.7 | 4.1 | 57.9 | 20.0 | 0.0 | 15.3 | 3.8 |
| $d_{x^2-y^2}$ | 40.0 | 55.5 | 0.0 | 1.9 | 41.7 | 17.1 | 24.7 | 3.5 | 8.4 |
| $d_{z^2}$ | 63.0 | 14.5 | 12.5 | 7.0 | 47.2 | 23.4 | 4.6 | 10.6 | 11.3 |

[a] Average O≡Mo−S−C = −121.1°. [b] Average O≡Mo−S−C = 51.1°.

## Analysis

The $MoOS_4$ first coordination spheres of **1** and **2** possess approximate $C_{4v}$ and $C_{2v}$ symmetry, respectively. The actual symmetry is lowered to $C_4$ in **1** by the synchronous pinwheel arrangement of the phenyl rings and to $C_2$ in **2** by the asynchronous dihedral angles enforced by the chelating biphenyl-2,2′-dithiolate ligand. The axial oxo ligand is an extremely strong $\sigma$ and $\pi$ donor and dominates the ligand field such that the Mo $d_{xy}$ orbital is lowest in energy and singly occupied.[43] Furthermore, the strong $\pi$-donor properties of the terminal oxo ligand result in a large energy splitting between the $d_{xy}$ orbital and the $d_{xz}$ and $d_{yz}$ orbitals (these are the $t_{2g}$ orbitals in $O_h$ symmetry) and assist in maintaining near degeneracy of $d_{xz}$ and $d_{yz}$. This large $d_{xy}$−$d_{xz,yz}$ splitting is characteristic of oxomolybdenum complexes and ranges from ∼13 000 to ∼16 000 $cm^{-1}$.[3−6,44,45] Thus, LMCT transitions to $d_{xz,yz}$ must occur at energies which are at least 13 000 $cm^{-1}$ higher than the lowest energy LMCT transitions to $d_{xy}$. We will limit our analysis of the absorption and MCD data to the energy region below 24 000 $cm^{-1}$, where electronic transitions which involve one-electron promotions to the $d_{xy}$ redox orbital are anticipated to occur.

**Oxomolybdenum Phenylthiolate Bonding.** There are two p orbitals on each thiolate S donor atom that are available for bonding to molybdenum. One of these orbitals is orthogonal to the phenyl-ring plane ($S^{\sigma}$), and the other is in the plane of the

---

(43) Nugent, W. A.; Mayer, J. M. *Metal−Ligand Multiple Bonds*; Wiley & Sons: New York, 1988.

(44) Sabel, D. M.; Gewirth, A. A. *Inorg. Chem.* **1994**, *33*, 148−156.

(45) Lever, A. B. P. *Inorganic Electronic Spectroscopy*, 2nd ed.; Elsevier Science Publishing: New York, 1986.

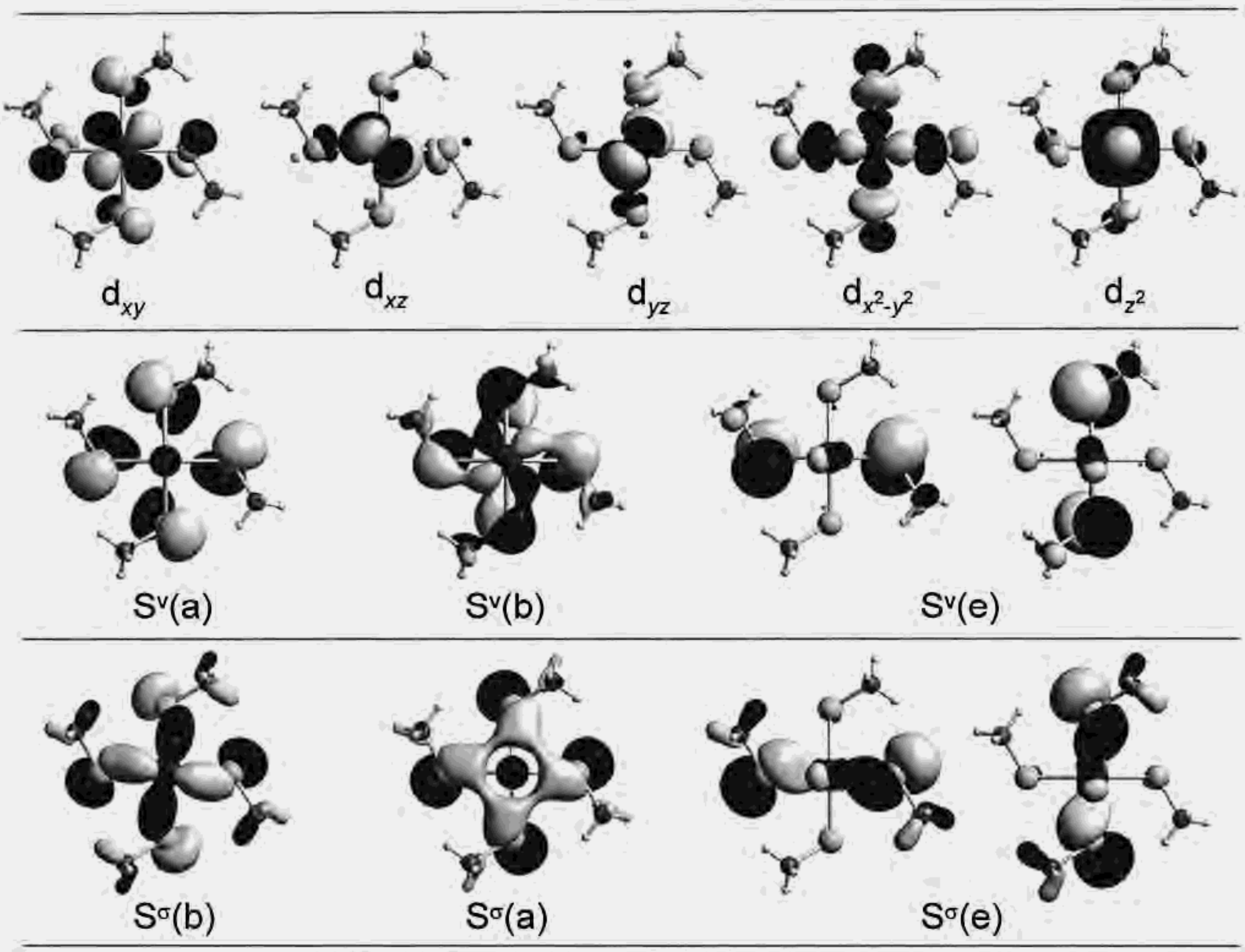

**Figure 5.** Electron-density contour plots resulting from DFT calculations on $[MoO(SCH_3)_4]^-$ using the crystallographic parameters of **1**. The view is oriented down the *z* axis (Mo≡O bond).

phenyl ring ($S^v$). The third p orbital on each sulfur donor is involved in $\sigma$ bonding with the phenyl-ring carbon and does not play a significant role in Mo−S bonding. The $S^\sigma$ orbitals are expected to be more energetically stabilized than the $S^v$ orbitals because of better overlap with the metal ($\sigma$ vs pseudo-$\sigma$ bonding), and this is corroborated by the DFT calculations (vide supra). Therefore, the intense low-energy bands observed in **1** and **2** are anticipated to arise from $S^v \rightarrow$ Mo $d_{xy}$ charge-transfer transitions.

The $S^\sigma$ orbitals form $\sigma$ bonds with $d_{x^2-y^2}$, and the degree of Mo−S overlap is dependent on the Mo−S−C angle (Figure 7). Maximum orbital overlap occurs at a Mo−S−C angle of 90° and decreases with an increase in the angle. This angle averages 110° in the crystal structure of **1**, whereas the structure of **2** displays two different Mo−S−C angles per $SPh-PhS^{2-}$ ligand that average 100 and 104°. The $S^v$ orbitals form pseudo-$\sigma$ bonds with $d_{xy}$, and the amount of orbital overlap is dependent on the O≡Mo−S−C dihedral angle. Maximum overlap occurs at a dihedral angle of 0° (Figure 8A), and the overlap is reduced to zero (nonbonding) as the dihedral angle approaches 90° (Figure 8C).[46] Comparison of the crystallographic data shows that the O≡Mo−S−C dihedral angle averages 58.8° for **1**, whereas **2** possesses two distinct angles averaging +51.5 and −121.1°. Interestingly, the DFT calculations suggest that the two sulfur atoms with dihedral angles averaging −121.1° donate considerably less electron density to Mo $d_{xy}$ than the two sulfur atoms with dihedral angles averaging 51.5° but donate substantially more electron density to Mo $d_{z^2}$. This charge donation would be anticipated to reduce the effective nuclear charge on the Mo ion of **2** relative to that of **1**. However, the O≡Mo−S−C dihedral angle is anticipated to vary in solution, and this could be substantial for **1** because its phenyl rings are not constrained with respect to rotation about the Mo−S bond.

**Resonance Raman Excitation Profiles.** Resonance Raman excitation profiles were constructed for both the 939 $cm^{-1}$ (Mo≡O) and 425 $cm^{-1}$ (Mo−S) vibrational modes of **1** (Figure 9). Significant enhancement of $\nu_{Mo\equiv O}$ is expected if the electronic transition involves a one-electron promotion to the Mo $d_{xz,yz}$ orbitals (out-of-plane Mo≡O $\pi$* antibonding), and enhancement of $\nu_{Mo-S}$ is anticipated for one-electron promotions to Mo $d_{xy}$ (in-plane Mo−S antibonding). The observed enhancement of the 425 $cm^{-1}$ Mo−S mode within the envelope of the intense low-energy absorption band indicates that these charge-transfer transitions result from one-electron promotions to Mo $d_{xy}$. Thus, the larger resonance enhancement of $\nu_{Mo-S}$ compared to that of $\nu_{Mo\equiv O}$ is consistent with the low-energy absorption band being comprised of S → Mo $d_{xy}$ LMCT transitions.[4]

**Band Assignments.** The Gaussian-resolved MCD and electronic absorption spectra of **1** and **2** are presented in Figures 10 and 11. The deconvolution of the absorption bands below 26 000 $cm^{-1}$ was accomplished by direct comparison with the Gaussian-

---

(46) The orbital overlap at a dihedral angle of 0° is $\pi$-type, but it becomes pseudo-$\sigma$ as the dihedral angle decreases until the orbitals become orthogonal (nonbonding) at 90°.

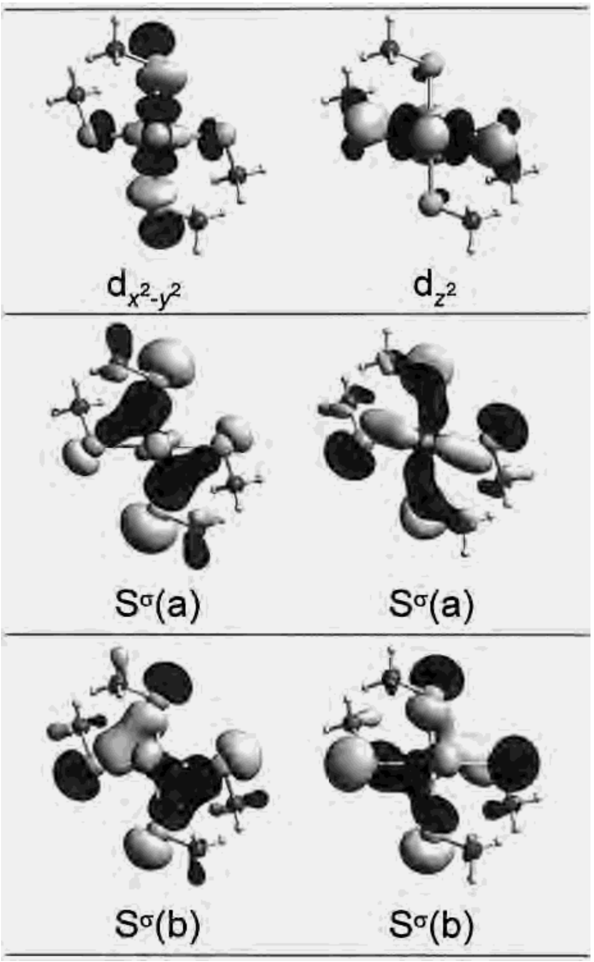

**Figure 6.** Electron-density contour plots resulting from DFT calculations on $[MoO(SCH_3)_4]^-$ using the crystallographic parameters of **2**. The view is oriented down the *z* axis (Mo≡O bond). Note the significant $C_2$ distortion of the Mo orbitals that interact with the $S^\sigma$ orbitals.

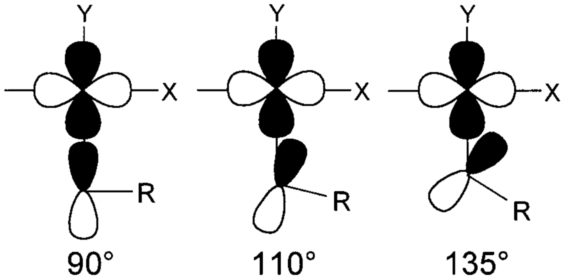

**Figure 7.** Effect of the Mo−S−C angle on $S^\sigma$−Mo $d_{x^2-y^2}$ orbital overlap.

resolved MCD bands. Because the MCD spectra were collected at a temperature of 5 K and the absorption spectra were collected at room temperature, the absorption bandwidths and energies were allowed to broaden and float (by a maximum of 500 $cm^{-1}$) during the fitting procedure relative to their corresponding MCD bands.[47] We will use effective $C_4$ symmetry for the band assignments of **1** and **2**. However, it should be noted that a $C_4 \rightarrow C_2$ reduction in symmetry results in e → b + b and b → a (see Figure 4).

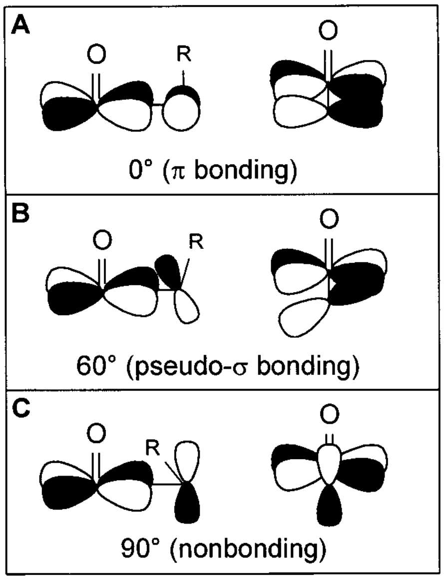

**Figure 8.** Effect of the O≡Mo−S−C dihedral angle on $S^v$−Mo $d_{xy}$ orbital overlap.

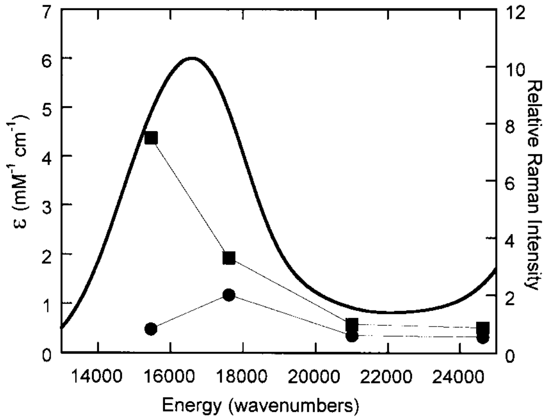

**Figure 9.** Resonance Raman enhancement profiles of the 425 $cm^{-1}$ Mo−S stretch (■) and the 939 $cm^{-1}$ Mo≡O stretch (●) of **1**.

**Bands 1 and 2.** Band 1 is the most intense component of the low-energy absorption feature and is assigned as $S^v(e) \rightarrow d_{xy}(b)$ based on the pseudo A-term MCD band shape and resonance enhancement of $\nu_{Mo-S}$. The $S^v(e) \rightarrow d_{xy}(b)$ transition is the only *x*,*y*-polarized transition involving the higher energy $S^v$ molecular orbitals, and transitions polarized along the Mo−S bonds are expected to be the most intense low-energy LMCT transitions. Band 2 is assigned as $S^v(b) \rightarrow d_{xy}(b)$ on the basis of the anticipated energetic stabilization of $S^v(b)$, via a bonding interaction with $d_{xy}(b)$, and the observed resonance enhancement of $\nu_{Mo-S}$ when using 568 nm (17 606 $cm^{-1}$) excitation.[48] The $S^v(b) \rightarrow d_{xy}(b)$ transition is a bonding → antibonding transition, and its intensity is a direct probe of the displacement of molybdenum above the $S_4$ plane (in the *z* direction). Although the $S^v(b)-d_{xy}(b)$ interaction is the dominant contributor to $S^v-d_{xy}$ bonding, the transition is *z*-polarized, and its intensity is proportional to the projection of the Mo−S bond onto the *z* axis (Mo≡O bond) of the molecule. The majority of the intensity of the low-energy absorption feature derives from these two transitions and is a direct indication of the amount of $S^v-d_{xy}$ orbital overlap. The Mo $d_{xy} \rightarrow d_{xz,yz}$ ligand-field transition is also expected to occur in the energy region spanned by band 2. However, we have not included this band in the fits because we observe no additional spectroscopic features in this energy region, and the MCD and absorption intensity is expected to

---

(47) Solomon, E. I. *Comments Inorg. Chem.* **1984**, *5*, 225−320.

(48) An alternative assignment has been proposed by McMaster et al. Their analysis of the spectra yield assignments for bands 1 and 2 which are reversed from ours. See ref 37.

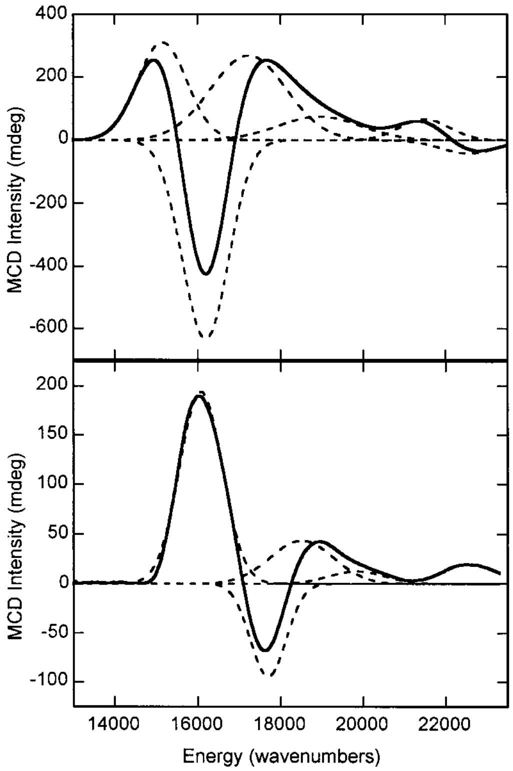

**Figure 10.** Gaussian-resolved MCD spectra of **1** (top) and **2** (bottom). The dashed lines represent the individual Gaussian bands used in the fit.

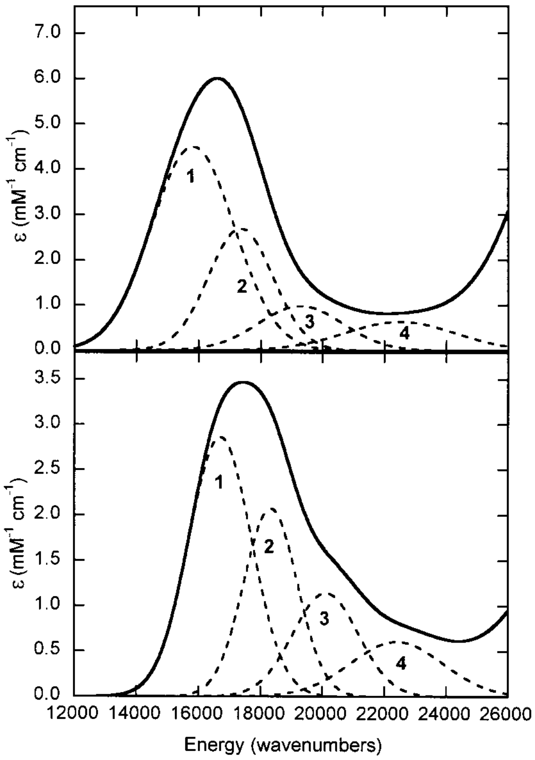

**Figure 11.** Gaussian-resolved electronic absorption spectra of **1** (top) and **2** (bottom). The dashed lines represent the individual Gaussian bands used in the fit. Note that the scale on the *y* axis in the upper figure is twice that of the lower figure.

be much weaker ($\epsilon < 50$ M$^{-1}$ cm$^{-1}$)[49,50] than those of the more intense LMCT transitions.

**Band 3.** The observed lower intensity of band 3 allows its assignment as S$^{v}$(a) → d$_{xy}$(b) because this transition is formally forbidden in $C_4$ symmetry. The higher energy of this transition results from the energetic stabilization of S$^{v}$(a) via bonding interactions with the oxo $\sigma$ orbital. Although this transition is forbidden in $C_4$ symmetry, it is allowed in $C_2$ symmetry, and small distortions toward $C_2$ symmetry allow this transition to gain some intensity. The greater intensity observed for this transition in the lower symmetry environment of **2** supports this argument.

**Band 4.** This band is assigned as S$^{\sigma}$(e) → d$_{xy}$(b) in **1** on the basis of the symmetric pseudo A-term MCD feature and the weak absorption intensity observed in this energy region. Further support comes from the absence of a corresponding pseudo A-term feature in the MCD spectrum of **2**. Only a single C-term MCD feature is observed for **2** in this energy region, providing direct experimental evidence of a low-symmetry splitting of the formally degenerate S$^{\sigma}$(e) orbital set in **2**. The experimental observation of S$^{\sigma}$(e) orbital splitting in **2** is corroborated by the DFT calculations (see Figure 4), which also indicate a splitting of the S$^{\sigma}$(e) molecular orbitals into two orbitals of b symmetry.

**Oscillator Strength Calculations.** Relative oscillator strengths for LMCT transitions to the lowest energy Mo d$_{xy}$ orbital were calculated from the S 3p orbital coefficients for the two molecular orbitals directly involved in a one-electron promotion yielding a given excited-state configuration.[4,51] Table 4 compares the calculated and experimental oscillator strengths for **1** and **2**. Because the Mo d$_{xy}$ orbital is an in-plane orbital (orthogonal to the Mo≡O bond), *x*,*y*-polarized transitions are anticipated to possess larger oscillator strengths than *z*-polarized transitions, given that the charge is transferred along the Mo—S bonds. The results of the DFT calculation for **1** show significant mixing of the in-plane and out-of-plane S p orbitals in the Mo d$_{xy}$ molecular orbital, and this leads to a larger calculated oscillator strength for the S$^{\sigma}$(e) → d$_{xy}$(b) transition than that which is determined experimentally. This mixing is not found in the calculation performed at the geometry of **2**. Thus, the dominant contributor to the absorption intensity of the low-energy feature results from the set of S$^{v}$ molecular orbitals which possess e symmetry in $C_4$, and the calculated oscillator strengths have been normalized to the experimental value for this transition. The observed experimental oscillator strengths for both *z*-polarized and formally forbidden charge-transfer transitions are higher than the calculated oscillator strengths, and this is most likely a result of lower symmetry distortions present in the solution environment.

## Discussion

Our results indicate that the dominant covalent interaction between thiolate donors and the Mo d$_{xy}$ redox orbital in oxomolybdenum thiolate complexes is the pseudo-$\sigma$ S$^{v}$—d$_{xy}$ interaction, and this is the origin of the lowest energy LMCT feature. Therefore, intensity differences in this band can be used to quantify the relative degree of S$^{v}$ → Mo d$_{xy}$ charge donation for various oxomolybdenum thiolate complexes. Specifically, the S$^{v}$—d$_{xy}$ orbital overlap is roughly proportional to the cosine of the O≡Mo—S—C dihedral angle ($\theta$), and this geometric parameter dictates the degree of S$^{v}$ → Mo d$_{xy}$ charge donation. Because the intensity of a charge-transfer band is proportional to $\langle M|L\rangle^2$ the relative intensities of these S$^{v}$ → Mo d$_{xy}$ bands should possess a $\cos^2(\theta)$ dependence.[47] This is depicted graphically in Figure 12. The integrated area of bands 1—3 for complex

---

(49) Pence, H. E.; Selbin, J. *Inorg. Chem.* **1969**, *8*, 353—358.

(50) Garner, C. D.; Lambert, P.; Mabbs, F. E.; King, T. J. *J. Chem. Soc., Dalton Trans.* **1977**, 1191—1198.

(51) Avoird, A.; Ros, P. *Theor. Chim. Acta* **1966**, *4*, 13—21.

**Table 4.** Comparison of Calculated and Experimental Oscillator Strengths

| | $[MoO(SPh)_4]^-$ (**1**) | | | | $[MoO(SPh\text{-}PhS)_2]^-$ (**2**) | | | |
|---|---|---|---|---|---|---|---|---|
| | $C_4$ symmetry | | oscillator strength | | $C_2$ symmetry | | oscillator strength | |
| band | transition | polarization | calculated | experimental | transition | polarization | calculated | experimental |
| 1 | $S^{\nu}(e) \rightarrow d_{xy}(b)$ | *x,y* | $6.5 \times 10^{-2}$ | $6.5 \times 10^{-2}$ | $S^{\nu}(b) \rightarrow d_{xy}(a)$[a] | *x,y* | $3.1 \times 10^{-2}$ | $3.1 \times 10^{-2}$ |
| 2 | $S^{\nu}(b) \rightarrow d_{xy}(b)$ | *z* | $5.4 \times 10^{-3}$ | $3.0 \times 10^{-2}$ | $S^{\nu}(a) \rightarrow d_{xy}(a)$ | *z* | $5.6 \times 10^{-4}$ | $1.9 \times 10^{-2}$ |
| 3 | $S^{\nu}(a) \rightarrow d_{xy}(b)$ | forbidden | | $1.4 \times 10^{-2}$ | $S^{\nu}(a) \rightarrow d_{xy}(a)$ | *z* | $1.3 \times 10^{-3}$ | $1.3 \times 10^{-2}$ |
| 4 | $S^{\sigma}(e) \rightarrow d_{xy}(b)$ | *x,y* | $6.8 \times 10^{-2}$ | $1.2 \times 10^{-2}$ | $S^{\sigma}(b) \rightarrow d_{xy}(a)$ | *x,y* | $7.6 \times 10^{-3}$ | $9.8 \times 10^{-3}$ |
| | | | | | $S^{\sigma}(b) \rightarrow d_{xy}(a)$ | *x,y* | $5.5 \times 10^{-3}$ | |
| | $S^{\sigma}(b) \rightarrow d_{xy}(b)$ | *z* | $4.6 \times 10^{-3}$ | | $S^{\sigma}(a) \rightarrow d_{xy}(a)$ | *z* | $4.4 \times 10^{-4}$ | |
| | $S^{\sigma}(a) \rightarrow d_{xy}(b)$ | forbidden | | | $S^{\sigma}(a) \rightarrow d_{xy}(a)$ | *z* | $5.7 \times 10^{-4}$ | |

[a] The two $S^{\nu}$ (b) components were summed because of the near degeneracy of the orbitals.

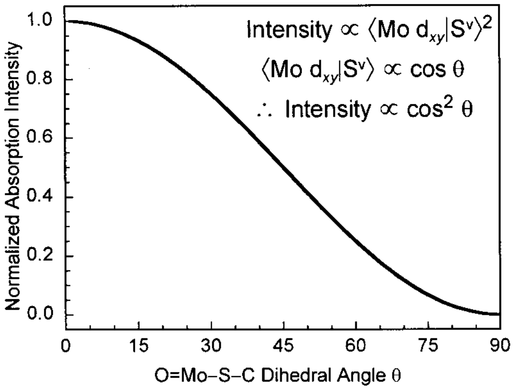

**Figure 12.** $\cos^2\theta$ dependence of the low-energy $S^v \rightarrow d_{xy}$ LMCT transition absorption intensity as a function of the O≡Mo—S—C dihedral angle ($\theta$).

**1** is approximately twice that of **2**, indicating $PhS^-$ is a considerably better pseudo-$\sigma$ donor than $SPh{-}PhS^{2-}$ in the solution geometries.[52] Similarly, the $S^{\sigma} \rightarrow$ Mo $d_{xy}$ charge donation may be directly probed via the intensity of the $S^{\sigma} \rightarrow$ Mo $d_{xy}$ charge-transfer transition (band 4) which occurs at higher energy (20 000−24 000 $cm^{-1}$). We find that the experimental intensities of the $S^{\sigma}(e) \rightarrow d_{xy}$ transition for **1** and the corresponding $S^{\sigma}(b) \rightarrow d_{xy}$ transition for **2** are weak and essentially identical for both complexes. This strongly suggests that differences in thiolate S−Mo $d_{xy}$ bonding are predominately a function of the $S^v{-}d_{xy}$ interaction. Thus, the *total* sulfur covalency contribution to the $d_{xy}$ redox orbital results from a combination of $S^v \rightarrow$ Mo $d_{xy}$ and $S^{\sigma} \rightarrow$ Mo $d_{xy}$ charge donation, and this directly affects the molybdenum reduction potential by raising the absolute energy of the $d_{xy}$ redox orbital and reducing the effective nuclear charge on the metal.

The S → Mo $d_{xy}$ charge donation in **1** and **2** results in a covalent reduction of charge localized on molybdenum, and this effect appears to be greatest for **1**. This is due to enhanced $S^v{-}d_{xy}$ covalency, which is revealed by the more intense low-energy charge-transfer transitions in the solution spectra of **1**. Therefore, it might be anticipated that **1** would be harder to reduce than **2** on the basis of this simple charge donation argument. However, this is not experimentally observed, because **1** is easier to reduce by ~120 mV. Provided that the differences in the reduction potential are solely related to electronic effects, bonding interactions involving the $S^{\sigma}$ orbitals and the Mo $d_{x^2-y^2}$ and $d_{z^2}$ orbitals must also be considered in the reduction of the charge localized on molybdenum. Unfortunately, these bonding interactions cannot easily be probed because the $S^{\sigma} \rightarrow d_{x^2-y^2}$, $d_{z^2}$ charge-transfer transitions occur at energies greater than 25 000 $cm^{-1}$ and are obscured by numerous overlapping charge-transfer bands. This makes definitive band assignments difficult. However, the relative effect of charge reduction on the metal is also reflected in the relative *energies* of the charge-transfer manifolds of **1** and **2**, and all of the observed S → Mo $d_{xy}$ charge-transfer transitions occur at higher energy in **2** compared with those in **1**. The DFT calculations indicate that a decrease in the effective nuclear charge on the Mo ion in **2** could result from the greater $S^{\sigma} \rightarrow$ Mo $d_{z^2}$ charge-donating ability of the $SPh{-}PhS^-$ ligand in the $C_2$ geometry, and this may be the origin of the negative shift in the reduction potential for this complex. Enhanced $S^{\sigma}{-}d_{z^2}$ interactions result from the significant 2-fold distortion present in **2**, which decreases the Mo−S−C angle and concomitantly increases the Mo−S $\sigma$ overlap (Figure 7). Finally, the reorganizational energy associated with geometric changes that occur upon reduction may make substantial contributions to the potential of the Mo(V)/Mo(IV) couple. Evidence for a reorganizational energy component is seen in the broader absorption features of **1** compared to those of **2**. This is anticipated to arise from heterogeneous broadening effects brought about by the greater torsional flexibility of the $PhS^-$ ligand in **1**. Reduction of a given Mo(V) complex to the corresponding Mo(IV) state results in a decrease in the effective nuclear (positive) charge localized on the metal. Because the O≡Mo—S—C dihedral angle carefully controls the degree of S → Mo $d_{xy}$ charge donation, it seems likely that a distortion along this mode would accompany reduction in order to reduce the amount of thiolate anion charge donated to the metal and stabilize the reduced Mo site. Therefore, the apparent inability of **2** to effectively distort upon reduction raises the energy of the reduced state of **2** relative to that of **1** and nicely explains the experimentally observed reduction potential differences.

In summary, $S^v \rightarrow d_{xy}$ charge donation is the dominant covalent interaction between the thiolate ligand orbitals and the Mo $d_{xy}$ redox orbital. We have shown that the lowest energy absorption bands in **1** and **2** arise from multiple $S^v \rightarrow d_{xy}$ charge-transfer transitions, and this provides a direct experimental probe of pseudo-$\sigma$ bonding contributions to Mo−S covalency. However, $S^v{-}d_{xy}$ covalency does not appear to be the dominant contributor to the observed differences in the reduction potentials of **1** and **2**, per se. This appears to arise from either increased $S^{\sigma} \rightarrow d_{x^2-y^2}$, $d_{z^2}$ charge donation in compound **2** or the ability of the coordinated thiolates to reorganize upon reduction and lower the total energy of the reduced Mo(IV) state.

**Relevance to SO.** The nature of Mo−S bonding in oxomolybdenum tetrathiolate complexes provides an excellent framework for developing insight into the specific role of the cysteine thiolate coordinated to molybdenum in SO. Studies on the C207S mutant of human SO[53] have shown that the coordinated cysteine is necessary for catalytic activity, yet the

---

(52) This trend is not reflected in the calculations. However, the calculations were performed using the solid-state geometries, which prevented contributions from distortions in solution that would increase the pseudo-$\sigma$ orbital overlap.

exact function of this residue remains unknown. One hypothesis is that anisotropic covalency contributions to $Mo-S_{Cys}$ bonding function to preferentially labilize one of the oxo ligands of the oxidized site, lowering the activation energy for the oxidation of sulfite.[54] Interestingly, the structure of chicken liver SO suggests that the pyranopterin may not function to provide an efficient ET pathway because it is not oriented in the direction of the b-type heme.[7] Therefore, an additional role for the coordinated cysteine may be to couple the active site into hole superexchange pathways for ET regeneration of the Mo(VI) site. This would require a considerable covalent interaction between $S_{Cys}$ and the Mo $d_{xy}$ redox orbital for maximum efficiency, and this covalency would result in the observation of an intense low-energy $S_{Cys} \rightarrow d_{xy}$ LMCT transition. Our calculations show that the sulfur character covalently mixed into the $d_{xy}$ redox orbitals of **1** and **2** is ~6% per sulfur donor. Although significant, this is substantially less than the 38% sulfur character mixed in the Cu $d_{x^2-y^2}$ orbital of poplar plastocyanin, which results from a very covalent $S_{Cys}-Cu\ d_{x^2-y^2}$ $\pi$-bonding interaction.[38] These differences in sulfur character per thiolate are a function of the $L_z-M-S_{Cys}-C$ dihedral angle (the $O\equiv Mo-S_{Cys}-C$ dihedral angle in SO) and indicate that the optimal geometry for coupling molybdenum into ET pathways that involve the coordinated cysteine is one where the $O\equiv Mo-S_{Cys}-C$ dihedral angle is 0°. However, the crystallographically determined $O\equiv Mo-S_{Cys}-C$ angle in chicken liver SO[7] is ~90°, resulting in the $d_{xy}$ and $S^{v}_{Cys}$ orbitals being orthogonal to one another and precluding a covalent interaction between them (Figure 8C). Therefore, there should also be no low-energy $S^{v}_{Cys} \rightarrow Mo$ charge-transfer transition in reduced SO, and MCD studies on the enzyme poised in the ET-relevant Mo(V) oxidation state show no evidence for a low-energy $S^{v}_{Cys} \rightarrow Mo$ band.[55] Furthermore, oxomolybdenum model compounds with constrained $O\equiv Mo-S-C$ angles of ~90° do not possess low-energy S → Mo charge-transfer transitions arising from the constrained thiolate.[56-58] We hypothesize that a severe reduction in $S_{Cys}-d_{xy}$ mixing in SO precludes an efficient ET pathway that directly involves the coordinated cysteine, and ET regeneration of the oxidized active site must be facilitated by the pyranopterin ene-1,2-dithiolate as we have previously proposed.[4-6] This would inevitably require the b-type heme domain to adopt a conformation in solution, relative to the active site, which differs from that observed in the X-ray structure. Thus, the cysteine ligation in SO most likely serves to modulate the effective nuclear charge of the molybdenum in order to appropriately poise the reduction potential for efficient ET regeneration of the Mo(VI) active site. However, because no appreciable orbital overlap appears to exist between $S_{Cys}$ and Mo $d_{xy}$ in reduced SO, the cysteine cannot directly affect the reduction potential by destabilizing the $d_{xy}$ redox orbital through antibonding interactions. As a result, the coordinated cysteine may indirectly modulate the molybdenum reduction potential via $S^{\sigma}_{Cys} \rightarrow Mo\ d_{x^2-y^2}, d_{z^2}$ charge donation as we have postulated for **1** and **2**. A reduced mono-oxo-Mo(IV) site is transiently formed in SO following oxygen atom transfer to sulfite, and the oxidized Mo(VI) site must be regenerated by two sequential one-electron transfers. Therefore, the ultimate result of $S^{\sigma}_{Cys} \rightarrow Mo\ d_{x^2-y^2}, d_{z^2}$ charge donation may be a covalent reduction of the effective nuclear charge on the metal, destabilizing the reduced Mo(IV) site and facilitating ET regeneration of the catalytically competent Mo(VI) state.

**Acknowledgment.** The authors thank Prof. John Enemark and Dr. Jonathan McMaster for useful discussions. M.L.K. thanks the National Institutes of Health for financial support of this work (Grant No. GM-057378). R.R.C. expresses appreciation to the University of Nevada, Reno, and NSF Nevada EPSCoR for funding.

**Supporting Information Available:** Plot of Mulliken charge versus $S-C-C'-S'$ torsion angle of the $SPh-PhS^{2-}$ ligand and figure of molecular orbital contour plots for **2** (analogous to Figure 6). This material is available free of charge via the Internet at http://pubs.acs.org.

IC0003729

---

(53) Garrett, R. M.; Rajagopalan, K. V. *J. Biol. Chem.* **1996**, *271*, 7387–7391.

(54) Izumi, Y.; Glaser, T.; Rose, K.; McMaster, J.; Basu, P.; Enemark, J. H.; Hedman, B.; Hodgson, K. O.; Solomon, E. I. *J. Am. Chem. Soc.* **1999**, *121*, 10035–10046.

(55) Helton, M. E.; Pacheco, A.; McMaster, J.; Enemark, J. H.; Kirk, M. L. *J. Inorg. Biochem.* **2000**, *80*, 227, 233.

(56) Mader, M. L.; Carducci, M. D.; Enemark, J. H. *Inorg. Chem.* **2000**, *39*, 525–531.

(57) Helton, M. E.; Kirk, M. L. Manuscript in preparation.

(58) Helton, M. E.; McNaughton, R. L.; Rubie, N. D.; Mader, M. L.; Enemark, J. H.; Kirk, M. L. Manuscript in preparation.